Pressure dependence of electron density distribution and *d-p-π* hybridization in titanate perovskite ferroelectrics

Takamitsu Yamanaka,[1,2,*] Yuki Nakamoto,[3] Muhtar Ahart,[4] and Ho-kwang Mao[2,5]

[1]*Department Earth and Space Science, Graduate School of Science, Osaka University, Osaka, Japan*

[2]*Center for High Pressure Science & Technology Advanced Research, 1690 Cailun Road, Pudon, Shanghai 201203, People's Republic of China*

[3]*Center of Quantum Science and Technology under Extreme Conditions, Osaka University, Osaka, Japan*

[4]*Institute of Materials Science and Department of Civil and Environmental Engineering, The George Washington University, Washington, DC 20052, USA*

[5]*Geophysical Laboratory, Carnegie Institution of Washington, Washington, DC 20015, USA*

(Received 10 December 2017; published 18 April 2018)

Electron density distributions of $PbTiO_3$, $BaTiO_3$, and $SrTiO_3$ were determined by synchrotron x-ray powder diffraction up to 55 GPa at 300 K and *ab initio* quantum chemical molecular orbital (MO) calculations, together with a combination of maximum entropy method calculations. The intensity profiles of Bragg peaks reveal split atoms in both ferroelectric $PbTiO_3$ and $BaTiO_3$, reflecting the two possible positions occupied by the Ti atom. The experimentally obtained atomic structure factor was used for the determination of the deformation in electron density and the *d-p-π* hybridization between d_{xz} (and d_{yz}) of Ti and p_x (and p_y) of O in the Ti-O bond. *Ab initio* MO calculations proved the change of the molecular orbital coupling and of Mulliken charges with a structure transformation. The Mulliken charge of Ti in the TiO_6 octahedron increased in the ionicity with increasing pressure in the cubic phase. The bonding nature is changed with a decrease in the hybridization of the Ti-O bond and the localization of the electron density with increasing pressure. The hybridization decreases with pressure and disappears in the cubic paraelectric phase, which has a much more localized electron density distribution.

DOI: 10.1103/PhysRevB.97.144109

I. INTRODUCTION

The prototype perovskite ferroelectrics $PbTiO_3$ (PTO) and $BaTiO_3$ (BTO) have been studied by both scientific and industrial communities because of their importance in modern ultrasonic and related devices [1–10]. The behavior of these materials raises fundamental questions in solid state physics. In particular, they serve as textbook examples of pressure- or temperature-induced soft phonon-driven structural transitions. In addition, because of the simplicity of their structures, they also serve as ideal tests for theory and first-principles calculations. Theoretical work has shown that the hybridization between the Ti $3d$ states and O $2p$ states is essential to the ferroelectric properties in both PTO and BTO [1], and that orbital hybridization exists between the Pb $6s$ state and O $2p$ states and plays a crucial role in the larger ferroelectricity observed in tetragonal PTO [11], whereas the interaction between Ba and O is almost ionic in tetragonal BTO [11,12]. One of the challenging tasks in this area of research is experimentally accessing the bonding electron distributions associated with the orbital hybridization in these materials.

First-principles calculations proposed the transition from ferroelectric to antiferroelectric distortion in the tetrahedral phase [3,4,5]. *Ab initio* molecular orbital calculations [6,7] were undertaken to elucidate the electronic structure and dynamical structure change. The elastic properties of $SrTiO_3$ (STO) in the cubic, tetragonal, and orthorhombic phases were also carried out using the *ab initio* pseudopotential method [8] and reported a cubic ($Pm\bar{3}m$)-to-tetragonal ($I4/mcm$) transition at 6 GPa, a tetragonal-to-orthorhombic ($Cmcm$) transition at 14 GPa, and an orthorhombic-to-monoclinic ($P2_1/m$) transition at 24 GPa. Here, we examine experimentally the pressure dependence of the electron density (ED) distribution in PTO and BTO using a combination of single-crystal diffraction and maximum entropy method (MEM) calculations [13,14]. The present measurements and analysis reveal the pressure-induced changes in the *d-p-π* hybridization originally predicted for these materials.

II. EXPERIMENT

Single-crystal diffraction measurements up to 12 GPa were performed using diamond anvil cells (DACs) and the synchrotron single-crystal x-ray diffraction facility at beam line BL-10A of the Photon Factory (KEK, Tsukuba, Japan) with a wavelength of $\lambda = 0.619\,07$ Å (20.0137 keV). Intensity measurements were carried out with a four-circle diffractometer using a fixed ϕ rotation and 100-μm collimator. A scintillation counter rather than imaging plate detector was used to measure diffraction intensities, because it is capable of much more precise intensity measurements and determination of the precise orientation matrix than an area detector. An orientation matrix (UB matrix) and unit cell parameters were determined by least-square fitting using the refined peak positions of 25 reflections.

*t.yamanaka@cap.ocn.ne.jp, takamitsu.yamanaka@hpstar.ac.cn

TABLE I. $PbTiO_3$ structure refinement. The numbers in parentheses denote errors of the last decimal. Atomic coordinate of Pb in the tetragonal phase is fixed to (000), because it is a noncentric structure. The position is placed for the origin of the structure of PTO. R (%) indicates the reliable factor ($R = \Sigma||F_{obs}|^2 - |F_{cal}|^2|/\Sigma|F_{obs}|^2$). B_{iso} (Å) is an isotropic temperature factor of the atom.

		Tetragonal						Cubic
		0.0001	1.0	3.3	6.0	9.3	10.3	11.9
a (Å)		3.9014(5)	3.9094(4)	3.8997(7)	3.8871(5)	3.8736(9)	3.8691(8)	3.861(1)
c (Å)		4.1466(7)	4.081(2)	4.026(2)	3.945(1)	3.890(2)	3.8797(9)	
V (Å^3)		63.11(2)	62.69(3)	61.22(9)	59.61(4)	58.37(20)	58.08(8)	57.5(1)
No_{obs}		2020	358	119	336	183	202	105
No_{used}		331	60	66	99	99	101	52
Pb	x	0	0	0	0	0	0	0
	y	0	0	0	0	0	0	0
	z	0	0	0	0	0	0	0
B_{iso} (Å^2)		0.938	0.906	0.889	0.783	0.809	0.770	1.826
Ti	x	0.5	0.5	0.5	0.5	0.5	0.5	0.5
	y	0.5	0.5	0.5	0.5	0.5	0.5	0.5
	z	0.5455	0.5386	0.5309	0.5292	0.5278	0. 5151	0.5
B_{iso} (Å^2)		0.374	0.233	0.312	0.349	0.399	0.378	0.396
O1	x	0.5	0.5	0.5	0.5	0.5	0.5	0.5
	y	0.5	0.5	0.5	0.5	0.5	0.5	0.5
	z	0.1218	0.1131	0.0942	0.0805	0.0652	0.0164	0.0
B_{iso} (Å^2)		0.619	0.543	0.665	0.675	0.686	0.582	2.090
O1	x	0.5	0.5	0.5	0.5	0.5	0.5	
	y	0	0	0	0	0	0.0	
	z	0.6282	0.6202	0.5998	0.5848	0.5724	0.5424	
B_{iso} (Å^2)		0.863	0.782	0.790	0.842	0.811	0789	
R (%)		4.13	4.32	5.06	3.22	3.84	4.81	6.77
wR(%)		4.75	2.48	4.20	3.14	3.43	4.04	8.00

Detailed specifications of this DAC are described in a previous report [15]. A mixture of ethanol, methanol, and water of 16:4:1 ratio was used as the pressure-transmitting medium, which guarantees hydrostatic conditions up to 12 GPa. Pressure was measured by the ruby luminescence method [16]. The high-pressure experiment is described in detail in the Supplemental Material [17].

X-ray powder diffraction experiments were also executed using DAC at pressures up to 55 GPa at ambient temperature. The lattice parameters of the samples were determined by Rietveld profile fitting from the observed diffraction peaks. The Rietveld refinement was conducted using the RIETAN-2000 program [18]. First, the background intensity distribution was adjusted for the refinement. The lattice constants, atomic positional coordinates, and temperature factors were then treated as variable parameters. Subsequently, the profile parameters and site-occupancy parameters were varied in the refinement. The full width at half maximum parameter, asymmetry parameters, and peak profile function confirmed that the diffraction data guaranteed a reliable profile analysis.

III. ANALYSIS AND RESULT

A. Structural refinements

To determine the effective charges of the constituent atoms of ferroelectric materials by x-ray diffraction, a conventional structural refinement was first carried out using the full matrix least-squares program RADY [19]. Reflections observed up to $2\theta = 75^\circ$ and with intensities of $F_0 > 3\sigma(F_0)$ were used for the least-squares refinements. Observed intensities were converted to structure factors after correction for x-ray absorption by the DAC, x-ray extinction, and Lorentz and polarization effects. Structure factors for reflections hkl were calculated by the atomic position $(x_s y_s z_s)$ for atom s of element j and atomic scattering factor f_j together with the displacement factor.

Atomic coordinates, site-occupancy parameters, anisotropic displacement factors, and isotropic extinction parameters were chosen as the variable parameters. The reliable parameter of the least-squares refinement is represented by $R(=w\Sigma||F_{obs}|^2-|F_{cal}|^2|/\Sigma|F_{obs}|^2)$. The factors of all present experiments were converged within $R = 0.05$. Since ferroelectric phases have a noncentrosymmetric structure, the origin of the structure of PTO and BTO was fixed at Pb(000) and Ba(000), respectively. The results of least-squares refinements for PTO and BTO are presented in Tables I and II, respectively.

Pb-O and Ti-O bond distances in PTO and Ba-O and Ti-O distances in BTO are presented in Table III. Figure 1 shows Pb-O and Ti-O bond lengths in PTO as a function of pressure. The difference in the two Pb-O2 and two Ti-O1 distances along the c axis becomes noticeably smaller in the tetrahedral ferroelectric phase with pressure. Their differences disappear in the cubic paraelectric phase. However, the four Pb-O1 and four Ti-O2 are not altered significantly by pressure. Above 12 GPa, PTO

TABLE II. $BaTiO_3$ structure refinement. All parameters in this table are the same as those in Table I.

Pressure			Tetragonal			Cubic
(GPa)		0.0001	0.4	2.5	4.3	5.8
a (Å)		4.0023(4)	4.0010(5)	3.9919(7)	3.9782(2)	3.9699(3)
c (Å)		4.0251(4)	4.0806(8)	3.9919(7)	3.9782(2)	3.9699(3)
V (Å^3)		64.48(1)	64.39(3)	63.61(3)	62.96(1)	62.57(2)
No_{obs}		1616	391	371	371	402
No_{used}		302	62	47	46	46
Ba	x	0	0	0	0	0
	y	0	0	0	0	0
	z	0	0	0	0	0
B_{iso} (Å^2)		0.447	0.494	0.390	0.381	0.377
Ti	x	0.5	0.5	0.5	0.5	0.5
	y	0.5	0.5	0.5	0.5	0.5
	z	0.4854	0.4904	0.5	0.5	0.5
B_{iso} (Å^2)		0.583	0.783	0.849	0.833	0.625
O1	x	0.5	0.5	0.5	0.5	0.5
	y	0.5	0.5	0.5	0.5	0.5
	z	0.1218	0.1131	0.0	0.0	0.0
B_{iso} (Å^2)		0.710	0.691	0.796	0.768	0.604
O2	x	0.5	0.5			
	y	0	0			
	z	0.5145	0.5066			
B_{iso} (Å^2)		0.624	0.717			
R (%)		1.32	4.66	4.88	4.90	3.87
wR (%)		2.15	3.36	3.80	3.79	3.99

adopts a cubic $Pm\bar{3}m$ structure, and all Pb-O and Ti-O bonds in the PbO_8 and TiO_6 polyhedra are respectively converged to equal values. For completeness, we also list the bulk modulus determined for the two materials [4,5]. The calculated data are $K_0 = 101(6)$ GPa, $K_0' = 4$ (fixed) for PTO, which are in good agreement with $K_0 = 107(3)$ GPa, $K_0' = 5.0(1)$ [9], and

TABLE III. Bond distances of $PbTiO_3$ and $BaTiO_3$. The numbers in parentheses denote errors of the last decimal. (Ti-O), (Ba-O), and (Pb-O) are average values of these bonds.

$PbTiO_3$							
			Tetragonal				Cubic
Pressure (GPa)	0.0001	1.0	3.3	6.0	9.3	10.3	11.9
Ti-O1	1.756(3)	1.7363(6)	1.758(8)	1.771(6)	1.800(9)	1.935(8)	
Ti-O1	2.390(4)	2.344(9)	2.268(1)	2.175(8)	2.091(1)	1.945(1)	
Ti-O2×4	1.981(2)	1.988(2)	1.970(3)	1.956(2)	1.945(1)	1.937(1)	
(Ti-O)	2.012	2.005	1.984	1.962	1.945	1.938	1.931
Pb-O1×4	2.805(2)	2.810(2)	2.784(3)	2.767(2)	2.751(5)	2.737(7)	
Pb-O2×4	2.486(3)	2.499(4)	2.529(5)	2.542(4)	2.553(7)	2.626(6)	
Pb-O2×4	3.254(4)	3.201(7)	3.113(9)	3.017(6)	2.951(9)	2.859(8)	
(Pb-O)	2.848	2.836	2.809	2.775	2.752	2.740	2.730

$BaTiO_3$					
	Tetragonal			Cubic	
Pressure (GPa)	0.001	0.4	2.5	4.3	5.8
Ti-O1	2.152(2)	2.091(8)			
Ti-O1	1.880(1)	1.930(8)			
Ti-O2×4	2.004(1)	2.001(2)			
(Ti-O)	2.008	2.004	1.996	1.989	1.985
Ba-O1×4	2.830(1)	2.824(2)			
Ba-O2×4	2.799(1)	2.851(6)			
Ba-O2×4	2.881(2)	2.817(6)			
(Ba-O)	2.837	2.834	2.823	2.813	2.807

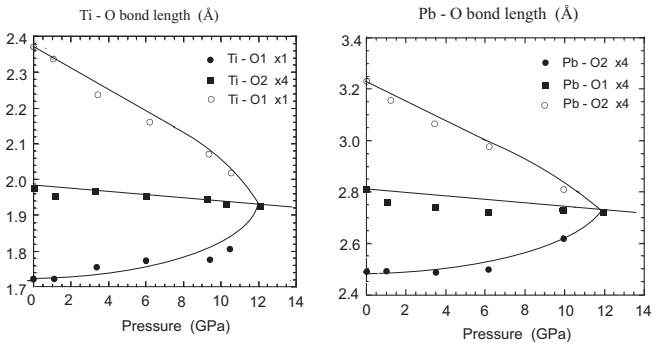

FIG. 1. Pressure dependence of Pb-O and Ti-O bond distance of two $PbTiO_3$ polymorphs: tetragonal phase at lower-pressure region and cubic phase at higher-pressure region. The observed errors are smaller than the symbols.

$K_0 = 154$ GPa, $K_0' = 4$ for BTO, a little larger than $K_0 = 135$ GPa, $K_0' = 6.4$ [8].

B. Maximum entropy method (MEM) analysis

Highly resolved distributions and atomic positional displacements are essential for understanding the electric polarization in ferroelectric materials. The Fourier series of the structure factors provides the ED distribution $\rho(xyz)$ in real space,

$$\rho(xyz) = \frac{1}{V}\sum_h\sum_k\sum_l F(hkl)\exp\{-2\pi i(hx+ky+lz)\}. \quad (1)$$

The difference Fourier synthesis $\{|F_{\rm obs}(hkl)|-|F_{\rm cal}(hkl)|\}$ is applied in order to disclose the deformation of the ED distribution. The residual ED $\Delta\rho(xyz)$ expresses the nonspherical deformation of the electron density, and is necessary, because the applied atomic scattering factor f_s is composed of the basically spherical distribution with $\sin\theta/\lambda$,

$$\Delta\rho(xyz) = \frac{1}{V}\sum_h\sum_k\sum_l\{|F_{\rm obs}(hkl)| - |F_{\rm cal}(hkl)|\} \times \exp\{-2\pi i(hx+ky+lz)\}. \quad (2)$$

The radial distribution of the ED distribution confirms the localization of electrons around atomic positions, which provides the dipole moment in a classical sense.

Fourier synthesis inevitably has a termination effect as a result of the limitations on the number of measured reflections. However, the difference Fourier synthesis can remove the termination effect in the observed ED distribution. The deformation electron density is obtained from the difference Fourier synthesis $|F_{\rm obs}(\boldsymbol{h})| - |F_{\rm cal}(\boldsymbol{h})|$ within reciprocal space defined by $\sin\theta/\lambda < 1.22$ at ambient pressure. However, the opening angle of the DAC restricts observed diffraction to small Q values. $F_{\rm obs}(hkl)$ in this limited reciprocal space cannot provide a precise residual electron density from the structure refinement by standard least-squares methods.

MEM statistically estimates the most reliable ED distribution from a finite set of observed structure factors, so the termination effect found in the Fourier synthesis is ignored. The method originated with Jaynes [20] and was subsequently applied to crystallographic problems from the standpoint of several experiments and theories [21–26]. The calculation method is described in the Supplemental Material [17]. A detailed discussion and procedure for using the single-crystal diffraction intensity data under high pressure in a MEM analysis were also described in our two earlier papers [13,14].

The data used in the MEM calculation are $F_{\rm obs}(\boldsymbol{h})$. In a single-crystal diffraction study these data are directly measured individually for all reflections. Consequently, the single-crystal diffraction intensity measurement can provide a much more precise ED distribution than the MEM analyses using powder diffraction intensities, because the former has no ambiguity in the deconvolution of the overlapping intensities often found in the powder diffraction pattern, along with a much larger number of observed $F_{\rm obs}(\boldsymbol{h})$.

The difference MEM calculation using $|F_{\rm MEM}(\boldsymbol{h})| - |F_{\rm cal}(\boldsymbol{h})|$ results in a more precise deformation electron density than does the difference Fourier synthesis. The residual ED distribution can be derived from the aspherical ED distribution such as may be produced by d electrons or the anharmonic thermal vibration of atoms. The anharmonicity is ignored in the present refinements, because the Debye temperatures Θ_D for PTO and BTO are much higher than room temperature.

The deformation electron density is observed in the tetragonal site symmetries, even though no initial structure model is applied in the MEM calculation. Although the diffraction angle of the DAC is limited to 80° in 2θ, the MEM guarantees a sufficiently reliable electron density around the atomic positions.

Because the MEM approach is statistical, it provides probability distributions that show the two possible positions for Ti atoms. The generated electron density map shows asymmetric features around these two positions of Ti and oxygen atoms of PTO and BTO. The split atoms are observed only in the direction of ⟨001⟩. However, they are not found in any direction perpendicular to ⟨001⟩, as presented in BTO (Fig. 2).

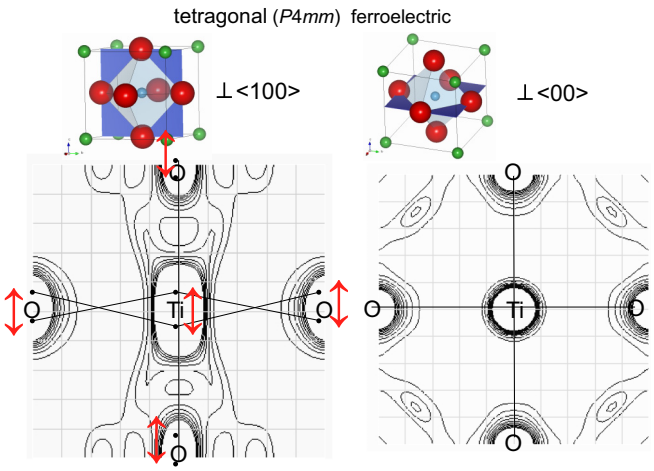

FIG. 2. MEM ED of $BaTiO_3$ derived from all reflections within $2\theta < 80°$ at ambient conditions. MEM $F_{\rm MEM}(\boldsymbol{h})$ is shown on plane (010) at $y = 0.0$ with a contour of 1.0 e Å^{-3} up to 10.0 e Å^{-3} with the origin at Ba (000). The red arrows represent the positional disorder of Ti and O atoms. The red arrow indicates the splitting of atoms.

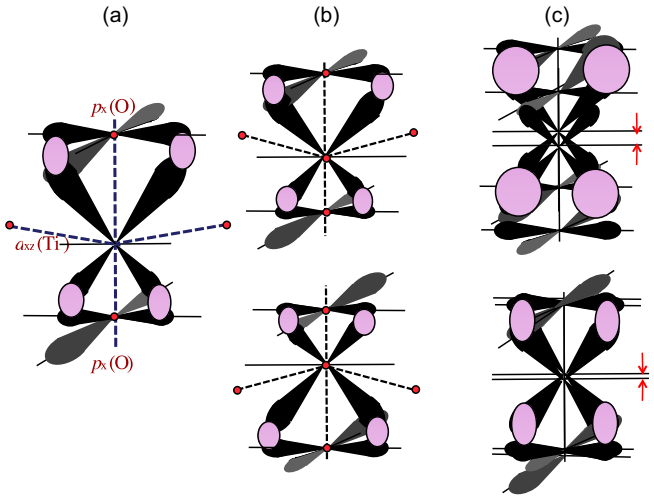

FIG. 3. d-p-π bond in two domains. (a) indicates the π bond in the single domain. (b) shows the individual π band in the split-atom model. (c) represents the apparent π bond in the statistically distributed domains, which is proved in the observed MEM map shown in Fig. 4. (c) Upper and lower maps present the electron density under low pressure and high pressure, respectively.

The split atoms are generated by long-range ordered atomic displacements. The localization of bonding electrons, lone-pair electrons, and an aspherical distribution of d electrons are considered. In the previous paper [10], the split atoms of Ti and O are proved in the Fourier synthesis for tetragonal PTO.

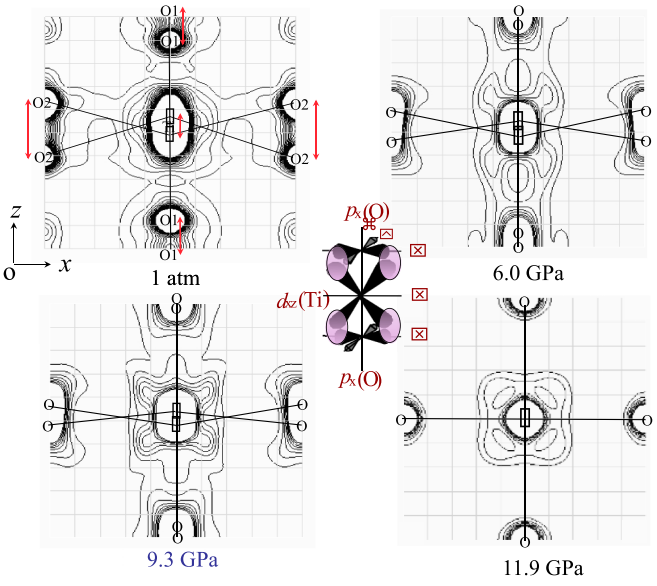

FIG. 4. MEM ED distribution of $PbTiO_3$ at $x = 0.5$ on the (100) plane with increasing pressure. Statistically split atoms of Ti and O are clearly found in the tetragonal phase, indicating polarization in the ⟨001⟩ direction. The deformation of the electron density is generated from d-p-π hybridization between Ti and apical O. ED map of the cubic phase at 11.9 GPa does not disclose the feature of the split atom. In contrast, the Ti-O bonds with four coplanar O show no hybridization.

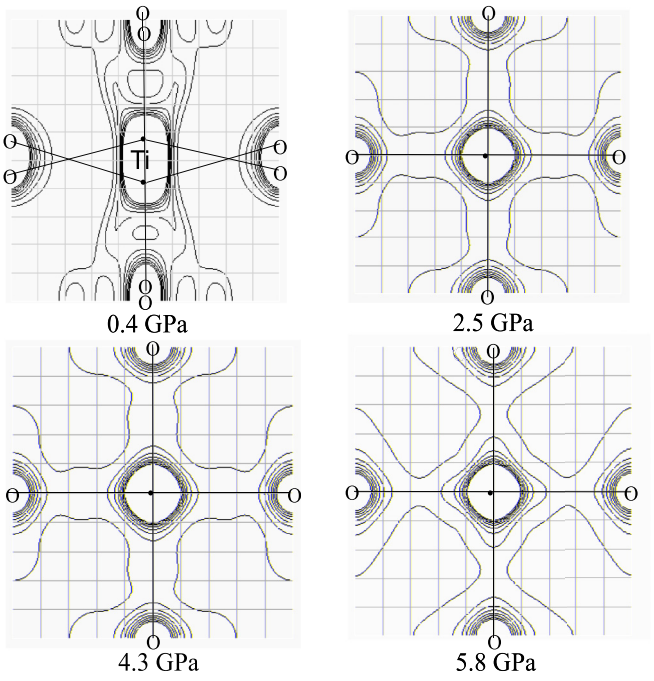

FIG. 5. MEM ED distribution of $BaTiO_3$ at $x = 0.5$ on the (100) plane with increasing pressure. Split atoms are observed only in the ED distribution at 0.4 GPa. The splitting is not found at pressures above 2.5 GPa. The tetragonal phase ($P4mm$, $z = 1$) transforms to the cubic paraelectric phase ($Pm\bar{3}m$, $z = 1$) at about 2 GPa. A contour of the projection is the same as in Fig. 2.

The present experiment reveals the splitting of these particular atoms decreases with increasing pressure.

The MEM ED distribution between Ti and O on the (010) plane of a tetragonal phase is schematically presented with the split atoms in Fig. 3.

The difference Fourier map confirms the d-electron orbit of Ti ($3d$) in the site symmetry of $m2m$, proving d_{xz} or d_{yz} in the t_{2g} group at the octahedral site. The residual electron density around Ti is clearly observed, indicating that hybridization of the d electron of Ti and the p electron of oxygen constructs the d-p-π bond. The present MEM maps experimentally prove the d-p hybridization between d_{xz} (and d_{yz}) of Ti and p_x (and p_y) of O1. However, a hybridization of d_{xy} of Ti and p_z of O2 of the coplanar atoms is not obviously observed at all pressures. From the split atoms in the tetragonal phase, an obvious deformation electron density is observed, confirming the possible polarization in the direction perpendicular to ⟨001⟩. But the two superposed domains indicate the opposite direction of deformation. The cubic phase of PTO at 11.9 GPa has no polarization in any direction perpendicular to the ⟨001⟩ direction, as shown in Fig. 4. The ED distribution around the Ti and O atoms is not contradictory to the centrosymmetric cubic site symmetries of $m\bar{3}m$, resulting in a paraelectric property without any deformation.

The ED maps of PTO (Fig. 4) and BTO (Fig. 5) with increasing pressure are given as projections on the (100) plane at $x = 0.5$ and the (001) plane at $z = 0.5$ in the region from 1 to 10 $e/\text{Å}^3$. These maps show the split atoms and statistical positional disorder, indicating polarization in the ⟨001⟩

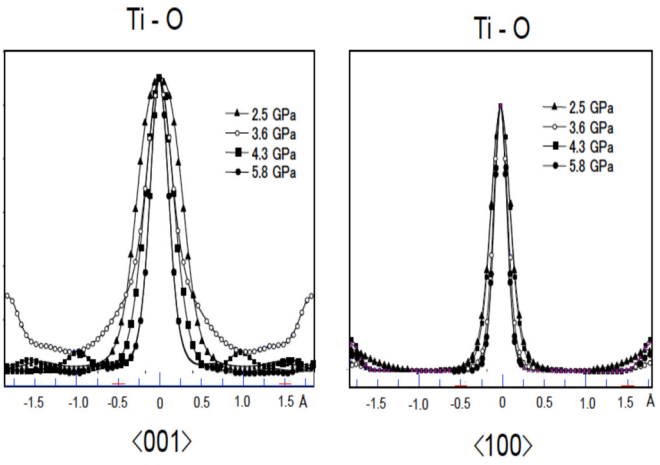

FIG. 6. Localization of electron density of the Ti atom in $BaTiO_3$. The radial distribution in the O-Ti-O bond in the MEM map is derived from all reflections within $2\theta < 80^\circ$ with increasing pressure. The radial distribution in Fig. 5 shows the localization of electron density of the cubic paraelectric phases is enhanced with pressure in the direction of ⟨001⟩, but almost no change in the localization is observed in the direction of ⟨100⟩ and ⟨010⟩.

direction. However, the maps projected on (001) at $z = 0.5$ indicate no polar character in the ⟨100⟩ and ⟨010⟩ directions. The Ti-O bond with apical oxygen O1 in the (100) projection at $z = 0.5$ reveals d-p-π bonding along z. In contrast, the four Ti-O bonds in the projection containing coplanar oxygen O2 indicate no d-p-π bond character. The pressure dependence of the ED distribution is presented for the tetragonal ferroelectric phase of PTO at 0.0001, 6.0, and 9.3 GPa and the cubic paraelectric phase at 11.9 GPa in Fig. 4. The split atom feature reflects the two possible positions occupied by the Ti atom. The splitting decreases with increasing pressure, disappears in the cubic paraelectric phase, and is accompanied with a more localized electron density. The radial ED distribution on the O-Ti-O bonds parallel to the z axis shown in Fig. 6 indicates that the localization of electron density around the Ti atoms is enhanced with pressure.

C. Effective charges

Atomic-scattering factors $f_i(\boldsymbol{h})$ are obtained from the Hartree-Fock wave functions (i.e., one-particle model). Thus, $f_j(\boldsymbol{h})$ gives an ideally spherical ED distribution for an isolated atom. $f_j(\boldsymbol{h})$ includes an anomalous dispersion, $f(\boldsymbol{h}) = f_0 + \Delta f' + i\Delta f''$. The effective charges of the atoms are obtained from the least-squares calculation by the shell model in which the core and valence electrons are separated. Inner-core electrons are frozen with respect to bonding effects according to the pseudopotential model, and only valence electron densities are deformed due to the coordination and thermal vibration of atoms. They are more sensitive to the interatomic potential affected by the coordination of the adjacent atoms.

A monopole refinement was applied instead of a multipole deformation density in this analysis. The κ parameter [27,28] was applied to the atomic-scattering factor to provide an indicator of the valence electron distribution around a given atom. The κ parameter used in this analysis is expressed as $\rho_{\text{valence}}(\mathbf{r}) = P_{\text{valence}}\kappa^3 \cdot \rho_{\text{valence}}(\kappa \cdot \mathbf{r})$, where $\rho_{\text{valence}}(\mathbf{r})$ is the ground-state density of the free atom. P_{valence} indicates the valence-shell population, which is the occupancy parameter of valence electrons. The perturbed valence electron density is

$$f(s/2) = \Sigma[P_{j,\text{core}} f_{j,\text{core}}(s/2) + P_{j,\text{valence}} f_{j,\text{valence}}(\kappa_j, s/2) + \Delta f'_j + i\Delta f''_j]. \quad (3)$$

The valence scattering of the perturbed atom at $s/2$ $(= \sin\theta/2\lambda)$ is given by

$$f_{\text{M-core}}(\kappa_j, s/2) = f_{j,\text{M-core (free atom)}}(\sin\theta/\lambda \cdot 1/\kappa_j). \quad (4)$$

The κ parameter was determined by the minimization of least-squares refinement using diffraction intensities of all reflections within $2\theta < 120^\circ$ at ambient conditions. The least-squares calculation starts from the neutral scattering factor ($\kappa = 0.0$) to determine the κ parameter.

In the case of $\kappa = 1$, the atomic-scattering factor is the radial distribution of neutral balance, which is the same as the factors found in the *International Tables for Crystallography* [29]. A value $\kappa > 1$ designates a localized valence electron density, implying more ionic bonding. On the other hand, $\kappa < 1$ characterizes a broad radial distribution of electron density, indicating more covalent bonding.

The effective charge q of atom j is the equivalent valence-shell population P_j, which is derived from the κ refinement,

$$q = -\int \Delta\rho(r)dr = -4\pi \int r^2\rho(r)dr. \quad (5)$$

The effective charges at ambient conditions are

$$q_{\text{Pb}} = +1.74, \quad q_{\text{Ti}} = +2.92, \quad \text{and} \quad q_{\text{O}} = -1.55 \quad \text{for } PbTiO_3,$$

$$q_{\text{Ba}} = +1.91, \quad q_{\text{Ti}} = +2.79, \quad \text{and} \quad q_{\text{O}} = -1.57 \quad \text{for } BaTiO_3.$$

More reflections used in the least-squares calculation give a more reliable κ parameter. Because of the limited number of reflections accessible experimentally as a result of the limited opening angle of the DAC, the κ parameter was not precisely able to resolve effective charges at high pressure.

The sum rule $\sum_i q_i = 0$ is fulfilled to within an error of 0.01 for both materials. The values are very similar to the Mulliken charges determined by *ab initio* calculations using Hartree-Fock (HF) and density functional theory [30], and suggest that BTO is slightly more ionic than PTO. The Mulliken effective charges of BTO and PTO obtained by seven different calculation methods [12] all indicate a noticeably covalent character; the present experimental results are similar to the HF calculations. For comparison, we also list effective charges obtained in the current work and relevant theoretical calculations by Evarestov *et al.* [30] in Table IV. Effective charges of Pb and Ba are compared.

IV. DISCUSSION

The difference Fourier map $|F_{\text{obs}}(\boldsymbol{h})| - |F_{\text{cal}}(\boldsymbol{h})|$ for BTO and PTO at ambient conditions has been determined by x-ray

TABLE IV. Effective charge defined by κ refinement. Basis sets of DFT and HF are used in the present calculation method by Evarestov *et al.* [30]. Mull and WTAO indicate Mulliken charge and Wannier-type atomic orbital (see their paper).

$BaTiO_3$		$PbTiO_3$	
Effective charge		Effective charge	
Ba	+1.91	Pb	+1.74
Ti	+2.59	Ti	+2.92
O	−1.50	O	−1.55

single-crystal diffraction [4], and ED distributions for PTO and BTO have been computed by first-principles calculations [11,12,31]. These theoretical results allow a visualization of the local ED distribution in an ideal unit cell and correspond to a case in which the ferroelectric pseudoparticle occupies one of the wells of a double-well potential. In our case, because we employed a statistical method, which provides a statistical average, we therefore observed split atoms—in fact, the split atoms indicate there are two possible positions for the Ti atom in the ferroelectric phase, and this is consistent with theory [31]. The present experimental results are consistent with the first-principles calculation [1], which first predicted a hybridization between d_{xz} (and d_{yz}) in the t_{2g} orbitals on Ti and p_x (and p_y) orbitals on the apical oxygen. The present experimental x-ray diffraction studies using single crystals of BTO and PTO elucidate the ferroelectric behaviors of the real bulk crystal.

The present investigation of the split atom makes a comparison with the previous eight-site model [32–34] which has been used to explain the successive ferroelectric transitions in BTO and $KNbO_3$ with temperature (see the Supplemental Material [17]). They observed strong streak-type diffuse scattering in their cubic phases; they also observed drastic changes in the diffuse scattering accompanying the relevant structural transitions with temperature. The eight-site model was proposed and used to explain the observed streak-type diffuse scattering. According to this model, the Ti cation in BTO can occupy eight sites in its cubic phase at high temperature. With decreasing temperature, BTO undergoes a paraelectric-to-ferroelectric transition. In our case, we focused on the intensity profile of each Bragg peak within the accessible reciprocal lattice space. We did not scan the space between Bragg peaks, and thus we did not observe streak-type diffuse scattering in our measurements.

According to the modern definition of polarization, spontaneous polarization arises from the flow of polarization currents in solids, which corresponds to the Berry phase of electronic wave functions, and can be interpreted as a displacement of the center charge of the Wannier functions (see, for example, Refs. [35,36]). Spontaneous polarization cannot be calculated directly from diffraction measurements, because information about the electronic wave functions is required. We obtained a statistical average of space and time of atomic vibrations and displacements and from this we calculated the effective charge (q) and polarized deviation ($\Delta\mathbf{r}$) of bond distances. Effective charges of atoms were obtained from the least-squares calculation based on the shell model.

In general, heavy atoms such as Pb and Ba in oxides show a small temperature factor in comparison with the oxygen atom. In this study, however, we observed the time and space average of dynamical phenomena due to atom disorder or microdomain disorder of PTO and BTO bulk structures. We found a large ED deformation around the Pb atom that is found along particular directions in the MEM maps. The displacement of Pb atoms is more noticeable than those of the Ti and O atoms, but these deformations disappear at higher pressures, where the ferroelectric structure transforms to a paraelectric structure. The transformation probably turns out, because the domain disorder or atomic displacement is homogenized or disappears above 11.9 GPa for PTO and 2 GPa for BTO.

ACKNOWLEDGMENTS

This work was sponsored by the Carnegie/DOE Alliance Center (CDAC, DE-FC52-08NA28554); DOE-BES (DE-FG02-06ER46280), and EFree, an Energy Frontier Research Center funded by the U.S. Department of Energy (DOE), Office of Science, Office of Basic Energy Sciences (BES), under Grant No. DESC0001057. H.K. Mao acknowledge the support of NSF EAR-1345112, 1447438, 1722515, and NSAF, China (Grant No. U1530402). Y.N. was partially supported by NSF EAR-1119504.

[1] R. E. Cohen, Nature (London) **358**, 136 (1992).
[2] Z. Wu and R. E. Cohen, Phys. Rev. Lett. **95**, 037601 (2005).
[3] M. Ahart, M. Somayazulu, P. Dera, H. K. Mao, R. E. Cohen, R. J. Hemley, R. Yang, H. P. Liermann, and Z. Wu, Nature (London) **451**, 545 (2008).
[4] R. H. Buttner and E. N. Maslen, Acta Crystallogr. B **48**, 764 (1992).
[5] S. A. Hayward, S. A. T. Redfern, H. J. Stone, M. G. Tucker, K. R. Whittle, and W. G. Marshall, Z. Kristallogr. **220**, 735 (2005).
[6] P. E. Janolin, P. Bouvier, J. Kreisel, P. A. Thomas, I. A. Kornev, L. Bellaiche, W. Crichton, M. Hanfland, and B. Dkhil, Phys. Rev. Lett. **101**, 237601 (2008).
[7] G. H. Kwei, A. C. Lawson, S. J. L. Billinge, and S. W. Cheong, J. Phys. Chem. **97**, 2368 (1993).
[8] P. Pruzan, D. Gourdain, J. C. Chervin, B. Canny, B. Couzinet, and M. Hanfland, Solid State Commun. **123**, 21 (2002).
[9] A. Sani, M. Hanfland, and D. Levy, J. Solid State Chem. **167**, 446 (2002).
[10] G. Shirane, R. Repinsky, and B. C. Frazer, Acta Crystallgr. **9**, 131140 (1956).
[11] Y. Duan, G. Tang, C. Chen, T. Lu, and Z. Wu, Phys. Rev. B **85**, 054108 (2012).
[12] S. Piskunov, E. Heifets, R. I. Eglitis, and G. Borstel, Comput. Mater. Sci. **29**, 165 (2004).
[13] T. Yamanaka, T. Okada, and Y. Nakamoto, Phys. Rev. B **80**, 094108 (2009).
[14] T. Yamanaka, M. Ahart, H.-k. Mao, and T. Suzuki, Solid State Commun. **249**, 54 (2017).

[15] T. Yamanaka, T. Fukuda, T. Hattori, and H. Sumiya, Rev. Sci. Instrum. **72**, 1458 (2001).
[16] H. K. Mao, T. Takahashi, W. A. Bassett, G. J. Kinsland, and L. Merril, J. Geophys. Res. **79**, 1165 (1974).
[17] See Supplemental Material at http://link.aps.org/supplemental/10.1103/PhysRevB.97.144109 for details of experimental methods, structural refinements, and MEM methods.
[18] F. Izumi and T. Ikeda, Mater. Sci. Forum **321–324**, 198 (2000).
[19] S. Sasaki and K. Tsukimura, J. Phys. Soc. Jpn. **56**, 437 (1987).
[20] E. T. Jaynes, IEEE Trans. Syst. Sci. Cybern. **4**, 227 (1968).
[21] G. Bricogne, Acta Crystallogr. A **44**, 517 (1988).
[22] D. M. Collins, Nature (London) **298**, 49 (1982).
[23] A. K. Livesey and J. Skilling, Acta Crystallogr. A **41**, 113 (1985).
[24] R. Narayan and R. Nityanada, Acta Crystallogr. A **38**, 122 (1982).
[25] J. Navaza, Acta Crystallogr. A **42**, 212 (1986).
[26] S. W. Wikins, J. N. Varghese, and M. S. Lehmann, Acta Crystallogr. A **39**, 47 (1983).
[27] P. Coppens, T. N. Guru Row, P. Leung, E. D. Stevens, P. J. Becker, and Y. W. Yang, Acta Crystallogr. A **35**, 63 (1979).
[28] R. J. van der Wal and R. F. Stewart, Acta Crystallogr. A **40**, 587 (1984).
[29] T. O. Hahn, *International Tables for Crystallography* (Reidel, Boston, 1983).
[30] R. A. Evarestov, V. P. Smirnov, and D. E. Usvyat, Solid State Commun. **127**, 423 (2003).
[31] R. E. Cohen and H. Krakauer, Phys. Rev. B **42**, 6416 (1990).
[32] P. R. Comes, M. Lambert, and A. Guinier, Acta Crystallogr. A **26**, 244 (1970).
[33] T. P. Dougherty, G. P. Wiederrecht, K. A. Nelson, M. H. Garrett, H. P. Jenssen, and C. Warde, Phys Rev. B **50**, 8996 (1994).
[34] S. Ravy, J. P. Itie, A. Polian, and M. Hanfland, Phys. Rev. Lett. **99**, 117601 (2007).
[35] R. D. King-Smith and D. Vanderbilt, Phys. Rev. B **47**, 1651 (1993).
[36] R. Resta, Rev. Mod. Phys. **66**, 899 (1994).